



Cite this: *J. Mater. Chem. A*, 2025, **13**, 24111

## Poly(styrene-co-maleamic acid)-based monoamide covalent adaptable networks<sup>†</sup>

Aitor Hernández, Susanne M. Fischer, Johan M. Winne and Filip E. Du Prez \*

This study presents poly(styrene-co-maleamic acid)-based monoamide (PS-MMA) covalent adaptable networks (CANs) as a novel class of high performance dynamic covalent polymer networks. PS-MMA CANs are readily synthesized by crosslinking poly(styrene-co-maleic anhydride) (PSMA) copolymers with secondary diamines, introducing a previously unexplored dynamic monoamide exchange chemistry. By tailoring the amine-to-anhydride ratios, crosslink density and viscoelastic properties were finely adjusted, yielding networks with high thermal stability and reprocessability. The dissociation of monoamides into amines and anhydrides, as observed in high-temperature FT-IR analysis, was validated through Density Functional Theory (DFT) calculations. These calculations revealed an enthalpically favored tendency for amines and anhydrides to re-associate into monoamides, confirming their suitability for thermally triggered dynamics and effective viscosity control at increasing temperatures. Rheological analysis of the PS-MMA CANs showed distinct diamine structure-dependent profiles, where the interplay between the chain entanglements, supramolecular interactions and dynamic dissociative monoamide debonding governed their stress relaxation regimes and macroscopic flow behavior. Notably, such materials exhibited a unique combination of fast dissociative relaxation modes and slower reptation-driven dynamics, enabling precise control over material properties. These networks demonstrated an exceptional thermal resilience, maintaining their integrity and flow properties at temperatures up to 280 °C, surpassing the chemically analogous (and more widely studied) monoester-based CANs. Lastly, chemical recycling experiments further validated the sustainability of PS-MMAs, enabling efficient recovery of PSMA precursors while preserving their functionality.

Received 12th March 2025  
Accepted 11th June 2025

DOI: 10.1039/d5ta02035b  
[rsc.li/materials-a](http://rsc.li/materials-a)

## Introduction

Covalent Adaptable Networks (CANs) are crosslinked polymer materials incorporating dynamic covalent bonds that rearrange when subjected to specific stimuli such as pH changes, light, ultrasonic waves, and most typically by heat.<sup>1–3</sup> This unique chemical architecture allows thermally triggered CANs to selectively exhibit the typical macroscopic flow properties of thermoplastics at high temperatures, while maintaining the structure and mechanical properties of thermosets at lower temperatures.<sup>4–6</sup> In this context, a series of dynamic covalent

chemistries have been developed exploiting neighboring group participation (NGP).<sup>7</sup> In that specific case, an internal catalytic effect can be derived from proximity-induced intramolecular covalent interactions, such as ring-closure reactions (e.g., monoester and dicarboximide/amide exchanges), where a fast intermolecular bond exchange is triggered by chemical moieties positioned near the dynamic covalent crosslink (see Scheme 1A).<sup>8–15</sup>

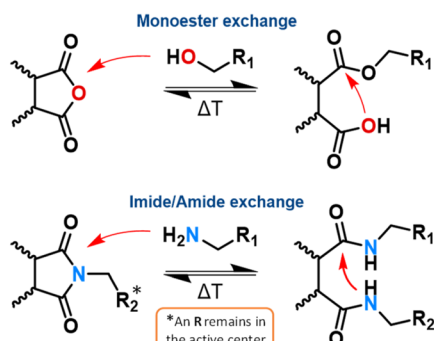
Our research group recently reported polystyrene (PS)-inspired dissociative CANs (PS-MMEs) synthesized *via* monoesters (Scheme 1A) derived from industrially applied poly(styrene-co-maleic) anhydride copolymers (PSMAs) and diol-based crosslinkers.<sup>16</sup> Such simple, yet functional material design facilitated the creation of NGP-assisted and chemically robust materials without the need for external catalysis while still offering fast flow rates and excellent (re)processability including extrusion and injection molding.<sup>16–18</sup> Indeed, the resulting architecture of PSMA-derived monoesters, embedded within the main chain of the copolymer and flanked by two styrene units, greatly improved the thermal resilience of these styrene-rich CANs compared to previous dynamic polyester/anhydride systems. Thus, PSMAs proved to be a polyvalent

*Polymer Chemistry Research Group, Centre of Macromolecular Chemistry, Laboratory for Organic Synthesis, Department of Organic and Macromolecular Chemistry, Faculty of Sciences, Ghent University, Krijgslaan 281 S4, Ghent B-9000, Belgium. E-mail: Filip.DuPrez@UGent.be*

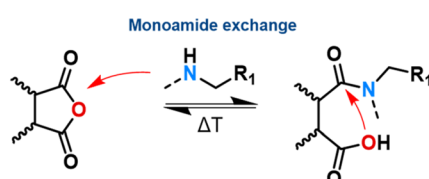
<sup>†</sup> Electronic supplementary information (ESI) available: Quick material reference appendix, glossary, reagents, instrumentation and characterization methods, synthetic procedures, GPC analyses, thermal analyses, dynamic mechanical thermal analyses, FT-IR analyses, <sup>1</sup>H-NMR analyses, SAOS measurements, stress relaxation measurements and analyses, creep measurements and analyses, single screw extrusion and injection molding experiments, network solubility, and chemical recycling procedures (PDF). See DOI: <https://doi.org/10.1039/d5ta02035b>



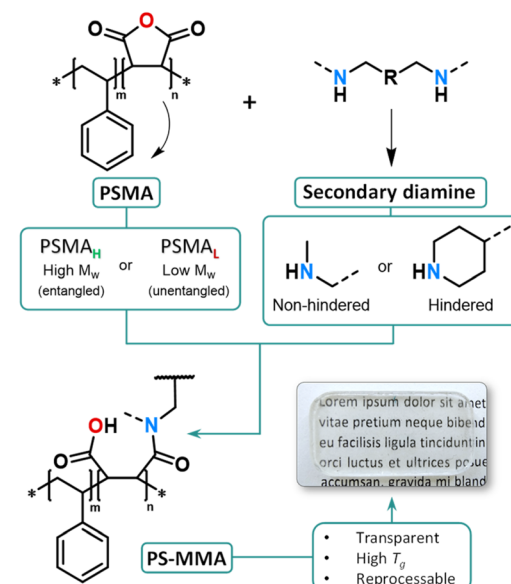
## A) Previous research:



## B) This work: Monoamides



## C) Study outline



**Scheme 1** (A) Reported dissociative crosslink rearrangement mechanisms involved in monoester and imide/amide dynamic exchanges at elevated temperatures. (B) Dissociative crosslink rearrangement mechanism involved in the herein reported monoamide dynamic exchange. (C) Overview of the strategy where PSMA copolymers, crosslinked with secondary diamines, are used to form poly(styrene-co-maleic acid) (PS-MMA) CANs.

synthetic handle to develop NGP-enabled CANs with robust chemical structures and could serve as a platform to explore other dynamic cross-linkers to reversibly ring-open and ring-close the maleic anhydride moiety.

The dynamic covalent exchange of amide bonds *via* NGP was reported in 2021 by two research groups including ours,<sup>13,14</sup> where bisamide/dicarboximide equilibria (derived from cyclic anhydrides or dibasic esters) enable an amide bond exchange (Scheme 1A). This would also appear as an interesting alternative chemistry platform to implement in PSMAs, considering the well-known high reactivity of primary amines towards anhydrides.<sup>19</sup> However, if the diol crosslinker strategy were to be simply substituted with primary diamines to obtain a bisamide CAN, the resulting PSMA network would entail a design flaw that incurs in reduced flow capability when compared to the earlier mentioned monoester-based design. Indeed, each bisamide pair would contribute to two crosslinking points per anhydride embedded in the PSMA chains (see Scheme 1A).

Then, as the dissociative mechanism is triggered, one of the crosslinking points per amide pair within the PSMA chain would remain part of the dicarboximide, resulting from the dissociative ring-closure of the amides. In this specific architecture, only a fraction of the network could simultaneously dissociate. In turn, this would limit the loss of crosslinking density that the CAN could experience, hence compromising the viscosity drop required to develop adequate flow rates and enable faster (re)processing times at normal PS processing temperatures.<sup>20–22</sup> Furthermore, the imide/amide dynamic exchange requires the presence of amide pairs that react to liberate primary amines upon dissociation. In other words,

formulations incorporating ratios  $[\text{NH}_2]/[\text{anhydride}] > 1$  would be needed in order to grant dynamicity to the system.<sup>13,14</sup>

Additionally, as seen in previous reports, it is certain that the presence of entanglements and elevated network connectivity in CANs synthesized from polymer precursors above their critical entanglement molecular weight ( $M_c$ ) have a large impact on the networks' rheological properties.<sup>16,23–27</sup> According to the Sticky Rouse and Sticky Reptation theory models,<sup>28,29</sup> the motion and flow mechanics of chain segments derived from entangled PSMAs ( $M_w > M_c$ )<sup>30–32</sup> are bound to exhibit chain segment dynamics that are constrained by temporary physical 'sticky' supramolecular or dynamic covalent interactions, following a snake-like reptation movement.<sup>33–35</sup> This situation leads to flow mechanics involving simultaneous processes where temporary associations continuously break and reform, establishing a complex interplay between entangled chain segment reptation movements, sticky interactions, and the relaxation of mechanical stress.<sup>36–38</sup>

Starting from this state-of-the-art and from our general interest in the design of amide-containing CANs for reasons of thermal stability and hydrolytic resistance,<sup>14,39</sup> the focus of this study was set in using secondary diamines as crosslinkers for the PSMA-embedded cyclic anhydride moieties. With this design strategy, cyclization to the cyclic imide is impossible (Scheme 1B), and at the same time a wide range of entangled CANs can be investigated by crosslinking commercial PSMAs, both below and above their  $M_c$ . These materials were expected to retain a CAN-character associated to the NGP effect of the unreacted, pendant carboxylic acid moiety that arises after ring opening. Moreover, as amide bonds are generally more robust



than ester bonds, we targeted a straightforward design of several robust, (re)processable polyamide networks with customizable properties. In fact, the resulting reversible so-called ‘amic acids’ or ‘monoamides’ within the poly(styrene-*co*-maleamic acid) CANs (PS-MMAs) closely resemble the previously studied monoester containing PS-MME CANs in which the ester functionality has been replaced with a tertiary amide that cannot form a dicarboximide (Scheme 1C). Finally, amide dissociation of conformationally restricted amic acid units within low molar mass compounds or crosslinked networks has been reported in strong acidic media<sup>40,41</sup> or in the presence of amine catalysts, facilitating carboxylate-mediated reactions enhanced by steric effects.<sup>42</sup> Alternatively, the herein reported PS-MMAs were studied as an alternative to imide/amide CANs generated from small molecule monomers to introduce a new class of catalyst-free amide based dissociative CANs.

## Experimental procedures

**Synthesis of PS-MMA CANs.** To a 250 mL or 1000 mL Teflon® beaker immersed in an oil bath and equipped with a magnetic stirrer, 3 mL of THF (or CHCl<sub>3</sub>) was added per gram of PSMA of commercial name Xibond® 120 (**PSMA<sub>H</sub>**) or Xibond® 220 (**PSMA<sub>L</sub>**) (Scheme 2A and Table 1). Afterwards, the PSMA beads were slowly poured into the beaker while stirring at room temperature, and the reaction setup was covered with aluminum foil. Once the beads had completely dissolved, targeting adequate stoichiometric ratios, the specified amount of secondary diamine [4,4-trimethylenedipiperidine (DPP) or *N,N*-dimethyl-1,6-hexanediamine (MeHDA)] (Scheme 2A and Table 1) was quickly added to the beaker at 0.2 g mL<sup>-1</sup> in THF (or CHCl<sub>3</sub>) solutions (Scheme 2B), and the beaker was covered again and kept under constant stirring for 5 min to let the organogel form slowly at room temperature. The resulting transparent gel was heated at 60 °C for 10 min before it was broken into small fragments (diameter <5 mm) inside the same Teflon® beaker with the help of a stainless steel lab spatula. Finally, the remaining solvent was removed by heating gel fragments inside the beaker in an oven at 80 °C for 1 h and then for 4 h under vacuum at 140 °C. PS-MMA CANs were obtained as

colorless (for NH/MA eq.  $\leq 0.5$ ) to faint yellow ([NH]/[MA] eq. = 1.00), glassy transparent materials.

## Solubility tests at room temperature

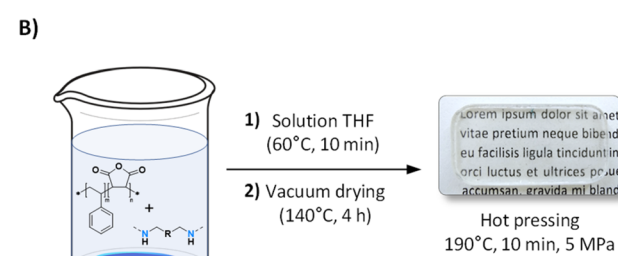
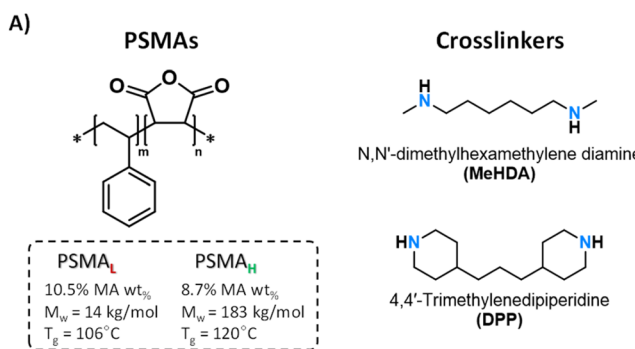
Solubility tests were performed on at least six discs, each with a thickness of 2 to 3 mm, prepared from preheated single-pressed samples using a 3 mm diameter puncher. These discs were annealed at 140 °C for 2 h and subsequently allowed to cool gradually. The samples were then immersed in 40 mL acetone for a period of 7 days in 40 mL vials, with the acetone being replaced on the 2nd, 4th, and 6th day, and weighed on the 7th day. The samples were then dried overnight under vacuum at 140 °C. The swelling ratios and soluble fractions were determined using eqn (1) and eqn (2), with  $m_0$ ,  $m_s$ , and  $m_d$  representing the initial, swollen, and dry masses of the samples, respectively.

$$\text{Swelling Ratio (\%)} = \frac{m_s - m_d}{m_d} \times 100 \quad (1)$$

$$\text{Soluble Fraction (\%)} = \frac{m_0 - m_d}{m_0} \times 100 \quad (2)$$

## Density functional theory (DFT) computational details

All calculations were performed using the quantum chemistry software ORCA (version 5.0.2).<sup>43</sup> Model compounds of the investigated structures were used in order to reduce the conformational freedom and the computational cost. All structures were optimized using the range-separated double-hybrid functional CAM-B3LYP<sup>44</sup> with Grimme’s D3 dispersion correction, and the def2-TZVPPD basis set<sup>45</sup> was employed for all atoms. A fine numerical integration grid was chosen for accurate energy and gradient evaluations. The conductor-like polarizable continuum model (CPCM)<sup>46</sup> was employed with *N,N*-dimethylformamide (DMF) as the solvent, providing an implicit representation of the matrix environment. Confirmation of the minima, calculation of zero-point vibrational energies and thermal property testing under standard conditions were performed by calculation of analytical normal modes using the rigid-rotor harmonic oscillator (RRHO)



**Scheme 2** (A) Structure and details of PSMA copolymers (left) and secondary diamine crosslinkers (right) used for the synthesis of the PS-MMAs studied (see Fig. S1† for GPC analysis). (B) Schematic representation of the PS-MMA synthesis method with a representative picture of a PS-MMA material (sample HDP<sub>50</sub>).



Table 1 Overview of the formulations used and thermal and physical properties of the synthesized PS-MMA CANs

CAN <sup>a</sup>	PSMA	Crosslinker	[NH]/[MA] <sub>eq./eq.</sub>	T <sub>g</sub> <sup>b</sup> (°C)	T <sub>d2%</sub> <sup>c</sup> (°C)	Swelling ratio (wt%)	Soluble fraction (wt%)
<b>LMe<sub>50</sub></b>	<b>PSMA<sub>L</sub></b>	MeHDA	0.50	127	300	87 ± 4	7.6 ± 2.7
<b>LMe<sub>100</sub></b>	<b>PSMA<sub>L</sub></b>	MeHDA	1.00	130	296	68 ± 3	5.0 ± 0.9
<b>LDP<sub>50</sub></b>	<b>PSMA<sub>L</sub></b>	DPP	0.50	124	313	88 ± 5	8.7 ± 3.0
<b>HMe<sub>10</sub></b>	<b>PSMA<sub>H</sub></b>	MeHDA	0.10	127	364	166 ± 8	6.8 ± 1.5
<b>HMe<sub>50</sub></b>	<b>PSMA<sub>H</sub></b>	MeHDA	0.50	132	342	90 ± 8	4.8 ± 0.7
<b>HDP<sub>10</sub></b>	<b>PSMA<sub>H</sub></b>	DPP	0.10	124	340	151 ± 8	5.2 ± 1.1
<b>HDP<sub>50</sub></b>	<b>PSMA<sub>H</sub></b>	DPP	0.50	124	338	81 ± 6	4.5 ± 1.1

<sup>a</sup> Systematic AB<sub>C</sub> network labeling code is explained at the beginning of the present subsection. <sup>b</sup> Glass transition temperature (T<sub>g</sub>) obtained from the second heating run measured by DSC (Fig. S3A and B). <sup>c</sup> Onset temperature after 2% mass loss measured by TGA (Fig. S4A and B).

approximation. The Nudged Elastic Band (NEB) method<sup>47</sup> was employed to locate transition states which were optimized using the abovementioned method. The Hessian matrix was recalculated after every 5th optimization step. All transition states displayed one imaginary frequency and were further confirmed by Intrinsic Reaction Coordinate (IRC) calculations.<sup>48</sup>

## Results and discussion

The in-solution synthesis of a series of PS-MMA CANs was performed starting from secondary diamines and two types of PSMA copolymers (Scheme 2A) with molar masses (see Fig. S1† for GPC analyses) either well below (**PSMA<sub>L</sub>**, low M<sub>w</sub>) or above (**PSMA<sub>H</sub>**, high M<sub>w</sub>) their expected critical entanglement molecular weight to study its influence on the material flow dynamics. The chosen diamine crosslinkers were incorporated in variable [NH<sub>2</sub>]/[anhydride] ratios to further evaluate the influence of the tertiary amide architecture and crosslink density on the viscoelastic and rheological properties of the PS-MMAs. As seen in Table 1, the PS-MMAs were labeled following an AB<sub>C</sub> code in which A stands for the polymer precursor used: 'L-Series' (**PSMA<sub>L</sub>**) and 'H-Series' (from **PSMA<sub>H</sub>**); B refers to the diamine crosslinker used: 'DPP' for the piperidine-based 4,4-trimethylenedipiperidine (DPP) and 'Me' for the methylamine-based N,N-dimethyl-1,6-hexanediamine (MeHDA). Lastly, the subscript C (*i.e.*, '100', '50', and '10') states the [NH]/[MA] equivalent percentage ratio as used in the PS-MMAs' formulation (see Schemes S1, S2, Tables S2 and S3† for further details and formulations).

All obtained PS-MMA CANs displayed soluble fractions below 10% (Table 1), elevated glass transition temperatures (*i.e.*, T<sub>g</sub> ≥ 120 °C, Fig. S3A and B†), high thermal stability (T<sub>d2% > 295 °C</sub>, Fig. S4A and B†), as well as exceptional thermal resilience, as evidenced by their good rheological property retention after prolonged exposure to elevated temperatures and excellent reprocessability (*vide infra*).

### Chemical and structural analysis *via* FTIR

Previous reports on PSMA-derived monoester networks demonstrated difficulties in achieving full conversion of anhydride to ester and carboxylic acid pairs due to kinetically arrested equilibria below the material's T<sub>g</sub>.<sup>16</sup> This was evidenced

by persistent ν (C=O, anhydride) stretches near 1780 cm<sup>-1</sup> in their FTIR spectra.<sup>9,16</sup> On the other hand, the FTIR spectra of the **LMe<sub>100</sub>** network ([NH]/[MA] eq. = 1.00, see Table 1) displayed residual anhydride ν (C=O, anhydride) peaks of much lower intensity compared to their homologue monoester networks (Fig. 1), which is ascribed to the higher nucleophilicity of amines towards the anhydrides.<sup>19</sup>

Mild intensity amide I carbonyl signals appeared between 1660 and 1610 cm<sup>-1</sup>, while intense absorption bands were always observed between 1760 and 1700 cm<sup>-1</sup>. Even though ν (C=O) of carboxylic acids generated in both monoesters and monoamides appeared between 1730 and 1700 cm<sup>-1</sup>, an intense overlapping band between 1760 and 1730 cm<sup>-1</sup> suggested a newly acquired carbonyl band associated with the monoamide's amic acid structure (further referred to as Monoamide I).

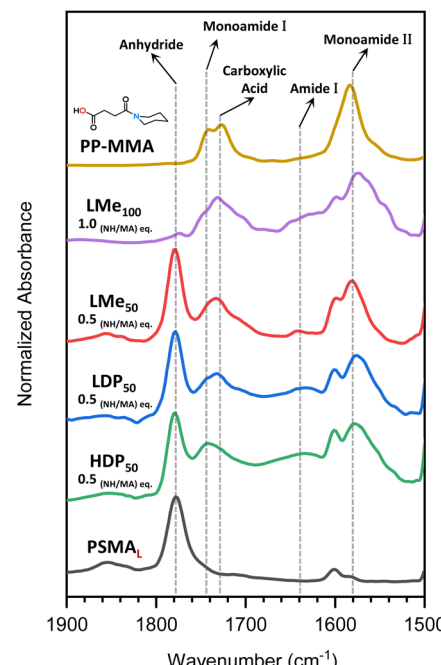


Fig. 1 Attenuated total reflectance-FTIR spectra showing the carbonyl stretch region of: model monoamide PP-MMA (yellow), LMe<sub>100</sub> (lavender), LMe<sub>50</sub> (red), LDP<sub>50</sub> (blue), HDP<sub>50</sub> (green) and the PSMA<sub>L</sub> prepolymer used as the reference (gray).



To further confirm this, a monoamide-containing model compound was synthesized from DPP and succinic anhydride (**PP-MMA**) (Scheme S4 and Fig. S2†). The FTIR spectrum of **PP-MMA** (Fig. 1) showcased a partial overlapping pair of peaks, composed of Monoamide I and  $\nu$  (C=O, carboxylic acid), centered at 1740 and 1725  $\text{cm}^{-1}$ , respectively, matching the values reported in the literature.<sup>49</sup> It appears that the molecular architecture of the maleamic acid groups in PS-MMAs leads to strong polar interactions between amide and carboxylic acids groups, resulting in a deviation from standard tertiary amide-related bands (still present in lower intensities). Additionally, a second intense signal was observed at 1585  $\text{cm}^{-1}$ , which is also attributed to the maleamic acid group Monoamide II.

### Monoamide dissociation mechanism

To gain further insights, the dissociation equilibrium of PS-MMA networks was evaluated between 100 °C and 200 °C via High Temperature Attenuated Total Reflectance FTIR (HT-ATR-FTIR) spectroscopy to follow changes in the molecular structure as well as assess the presence of intermediate species.

In contrast to previous reports on dissociative amide CANs,<sup>42</sup> the 'standard' Amide I carbonyl band in the HT-FTIR spectra of **LMe<sub>50</sub>** (Fig. 2A) remained unaltered with increasing temperature. In contrast, the carboxylic acid and Monoamide I bands demonstrated a clear decrease, while the intensity of the anhydride signals increased. These observations suggest a ring-closure reaction, where the neighboring carboxylic groups and tertiary amides react to regenerate the original cyclic anhydride.

In order to confirm the reaction mechanism, density functional theory (DFT) calculations, conducted at the CAM-B3LYP/def2-TZVPPD level of theory, have been made to investigate the formation of zwitterionic species during a classic nucleophilic acyl substitution process. This analysis was conducted for two types of aliphatic amines, representing the architecture around the amine groups of DPP and MeHDA: piperidine and dimethylamine (Fig. 2B).

Starting from the dissociated anhydride and amine, the proposed reaction begins with the direct addition of the neutral amine to the anhydride through a first transition state (TS1), resulting in the formation of a zwitterionic intermediate (**Int-1**). The energy barrier for the transition state involved was calculated to be 14.4  $\text{kJ mol}^{-1}$  higher for the piperidine when compared to the dimethylamine, likely due to the greater steric hindrance imposed by the piperidine's six-membered cycloaliphatic structure. A subsequent proton transfer step then leads to the stabilization of **Int-1**, and the formation of another intermediate (**Int-2**). The stabilization energy was determined to be 24.6  $\text{kJ mol}^{-1}$  for piperidine and 13.3  $\text{kJ mol}^{-1}$  for dimethylamine, suggesting that the charge separation in the zwitterion in **Int-1** is particularly less stabilized when the cycloaliphatic amine is involved due to the positive charge delocalization restrictions set by its cyclic structure. A stronger acidic character and lower stability of the piperidinium ion compared to dimethylammonium can be reasoned by comparing the  $\text{p}K_{\text{aH}}$  values of dimethylamine's ( $\text{p}K_{\text{aH}} = 19$ ) and piperidine's ( $\text{p}K_{\text{aH}} = 15$ ) ammonium cations in a non-aqueous medium like acetonitrile.<sup>50</sup> Thus, the stronger base is also the most reactive amine.

The transition from **Int-2** to the ring-opened structure (**Int-3**) occurs through a second transition state (TS2), with energy barriers of 67.9  $\text{kJ mol}^{-1}$  for piperidine and 53.3  $\text{kJ mol}^{-1}$  for dimethylamine, respectively. It is noteworthy that the similarity in energy between **Int-2** and **Int-3** underscores a high degree of reversibility in this step. The final step of the modelled reaction involves another proton transfer, leading to the formation of the monoamide product. Interestingly, in the reaction mechanism involving piperidine, the rate-determining step is the initial addition of the amine to the anhydride, while for dimethylamine, it is the ring-opening of **Int-2**. Such differences in rate-determining steps can be attributed to the structural and steric variations between the two types of secondary amines. It is noteworthy that the ring closure for the monoesters is expected to be much less endothermic than the corresponding ring

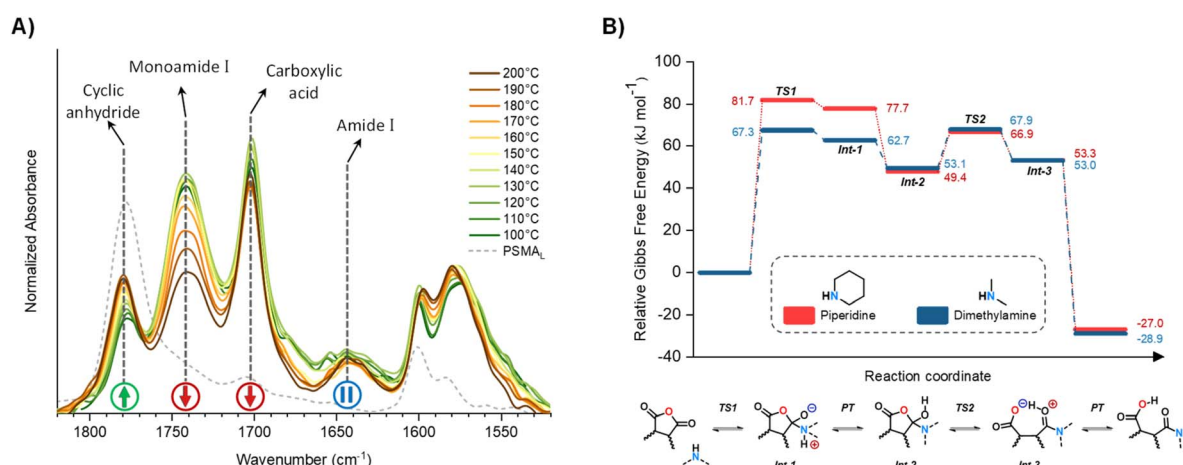


Fig. 2 (A) High temperature attenuated total reflectance-FTIR spectra of **LMe<sub>50</sub>**, showing the evolution of its carbonyl stretch peaks with increasing temperature. (B) Relative Gibbs free energies ( $\text{kJ mol}^{-1}$ ) calculated at the CAM-B3LYP-D3/def2-TZVPPD level of theory and reaction pathways for dimethylamine and piperidine. PT = proton transfer (not modelled).



closure of the monoamides, which indicates a much higher degree of reversibility in this step.<sup>51</sup>

Despite the structural and mechanistic similarities between monoesters and monoamides, these results reveal notable differences in their viscoelastic and dynamic properties. In essence, these calculations further highlight the enthalpically favored re-association of dissociated amines to monoamide moieties, pointing to the presence of effectively crosslinked structures at elevated temperatures in monoamide CANs. As seen in the literature, monoester dissociative CANs are prone to experiencing significant modulus and viscosity drops with increasing temperatures due to substantial net-crosslink density losses.<sup>16,51</sup> In contrast, monoamides, while still dissociating at higher temperatures, are bound to display a notable exothermic character according to their  $\Delta_r G^\circ$  (*ca.* +30 kJ mol<sup>-1</sup>). Such higher reactivity suggests greater re-association rates in MMAs and points to the preservation of network connectivity in PS-MMMAs, even at elevated temperatures. Consequently, PS-MMMAs are expected to physically behave closer to associative CANs, where their stress relaxation and viscosity drops are likely associated with short-lived bond dissociations. This in turn

results in effective network topology rearrangements in response to external mechanical stimuli, rather than in structural losses.

### Network rheological assessment

**Small amplitude oscillatory shear (SAOS) analysis.** The effect of the reversible crosslinks on the viscoelastic properties of the PS-MMMAs was evaluated *via* SAOS frequency sweep experiments by following the evolution of their storage ( $G'$ ) and loss ( $G''$ ) moduli. Different temperature ranges were chosen, between 210 and 160 °C for the ‘unentangled’ L-Series (Fig. 3A and C) and 240–160 °C for the more elastic ‘entangled’ H-Series (Fig. 3B and D), considering the stronger impact of rising temperatures over the viscosities of the faster flowing L-Series networks.

As further discussed below, common features shared between all PS-MMMAs include apparent  $G'$  plateaus ( $G'_p$ ), typical for efficiently crosslinked networks at intermediate frequencies (see Table 2 for  $G'_p$  values at 160 and 200 °C), and a dominant viscous character at low frequencies where  $G' < G''$  at high temperatures starting at 180 °C for  $\text{PSMA}_L$  and at 220 °C on  $\text{PSMA}_H$ -derived materials, respectively.<sup>22,52,53</sup> However, different

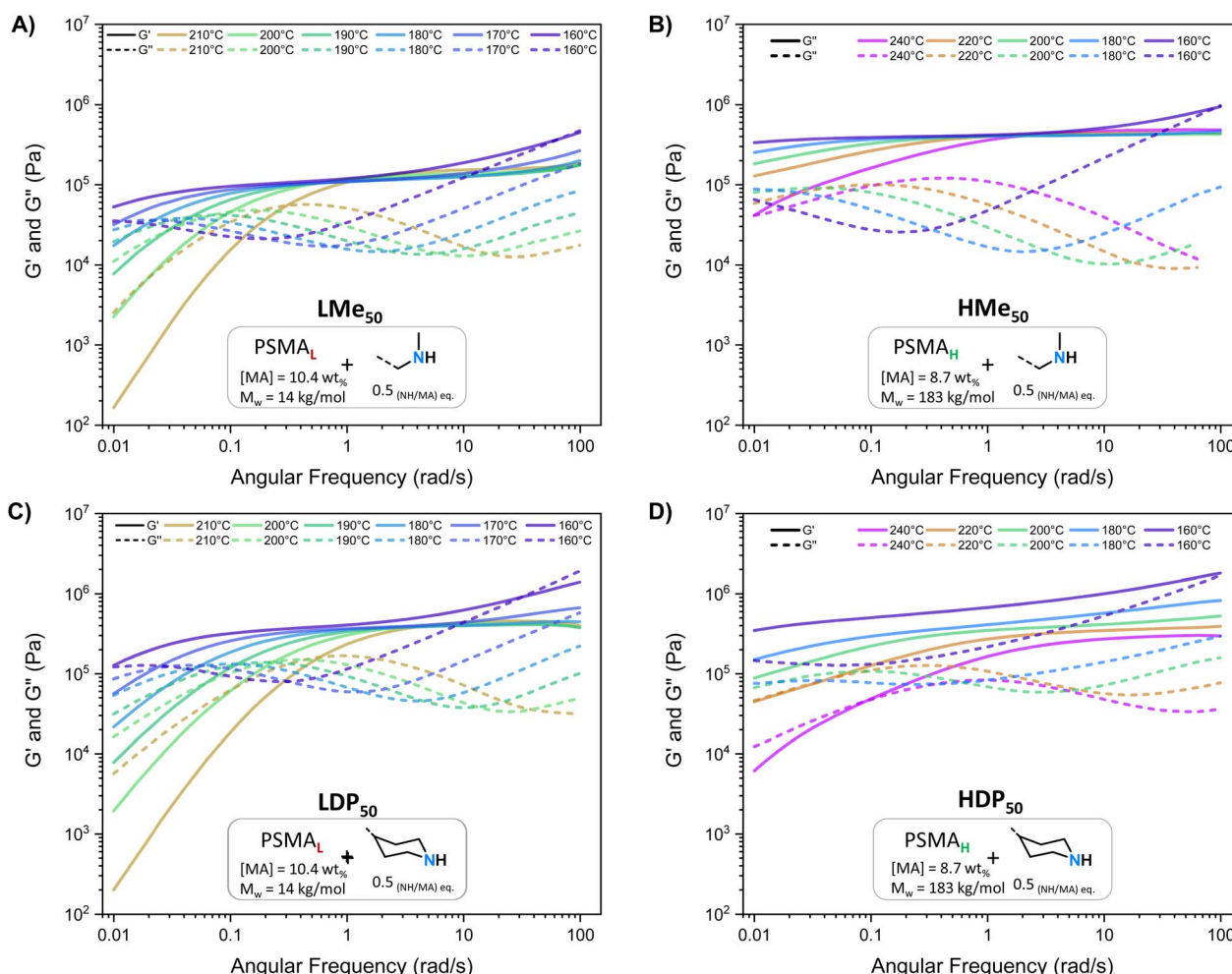


Fig. 3 SAOS measurements ranging from 210 to 160 °C of the  $\text{PSMA}_L$  derived PS-MMA networks: (A)  $\text{LMe}_{50}$  and (C)  $\text{LDP}_{50}$ . SAOS measurements ranging from 240 to 160 °C of  $\text{PSMA}_H$  derived PS-MMA networks: (B)  $\text{HMe}_{50}$  and (D)  $\text{HDP}_{50}$ .



Table 2  $G'_p$  values of PS-MMA networks at 200 and 160 °C

CAN	$G'_{p(200\text{ }^\circ\text{C})}$ (kPa)	$G'_{p(160\text{ }^\circ\text{C})}$ (kPa)
LMe <sub>50</sub>	115	120
LMe <sub>100</sub>	460	590
LDP <sub>50</sub>	390	410
HMe <sub>10</sub>	60	120
HMe <sub>50</sub>	460	490
HDP <sub>10</sub>	90	180
HDP <sub>50</sub>	390	670

$G'_p$  evolution profiles were observed when altering the PS-MMA formulations.<sup>54</sup>

As deduced from the DFT calculations, the unentangled networks derived from **PSMA<sub>L</sub>** (e.g., **LMe<sub>50</sub>** or **LDP<sub>50</sub>**, Fig. 3A and C) displayed minimal crosslinking density losses, as evidenced by quasi-invariable  $G'_p$  as a function of temperature. In fact, the sole difference observed for this **L**-Series of networks was the higher plateau moduli recorded for DPP-containing materials as a consequence of their different molecular architecture. Similarly, quasi-invariable  $G'_p$  values have also been observed in other dissociative CANs (e.g., imine/amide networks) that display ring-size related entropic factors, which favor the shift of their thermodynamic equilibrium towards the associated state.<sup>14</sup>

In the case of PS-MMAs, the static  $G'_p$  aligns with the conclusions drawn from the DFT calculations (*vide supra*) and points towards a strong enthalpic driving force that promotes a quick re-association, thereby maintaining a network structure that practically responds like an associative system if analyzed from a practical standpoint.<sup>21,22</sup> In the entire **H**-Series, such invariable  $G'_p$  (Table 2) was observed throughout the entire temperature range for the MeHDA-derived **HMe<sub>50</sub>** (Fig. 3B). This network displayed a plateau that was approximately 300 kPa higher than its **L**-Series counterpart (i.e., **LMe<sub>50</sub>**), which is ascribed to the structural reinforcement effect resulting from the additional chain entanglements. However, while the  $G'_p$  values of the DPP-derived **LDP<sub>50</sub>** and **HDP<sub>50</sub>** above 200 °C did not extensively differ (Fig. 3C and D), at 160 °C, the entire  $G'$  range of **HDP<sub>50</sub>** increased roughly to 250 kPa, similar to the difference observed between the  $G'$  values of **LMe<sub>50</sub>** and **HMe<sub>50</sub>**. Interestingly, as the MeHDA crosslinker content was further decreased in the formulation of the less crosslinked **HMe<sub>10</sub>** (Fig. S7C†), the profiles and values of its SAOS curves matched with those of its DPP-based counterpart at all temperatures (**HDP<sub>10</sub>**, Fig. S7C†). In other words, the chosen amine crosslinker's structure, parent copolymer, and the subsequent overall network connectivity have a direct impact on the resulting SAOS profile of the PS-MMAs.

**Stress relaxation analysis.** Subsequently, the stress relaxation and creep behavior of different synthesized PS-MMA networks were analyzed and compared to investigate how the intrinsic network connectivity impacts the material's relaxation behavior as well as their viscosity and terminal flow profiles.<sup>22,24</sup> These experiments were performed with a particular focus on understanding the presence of discrete relaxation regimes and the potential manifestation of sticky Rouse and reptation models

that have been previously reported in PSMA-derived monoester materials,<sup>16</sup> especially in entangled networks of elevated cross-linking density.

The unentangled **L**-Series PS-MMA networks consistently exhibited monomodal relaxation profiles across the tested temperature range (*i.e.*, 220 to 160 °C), where the only

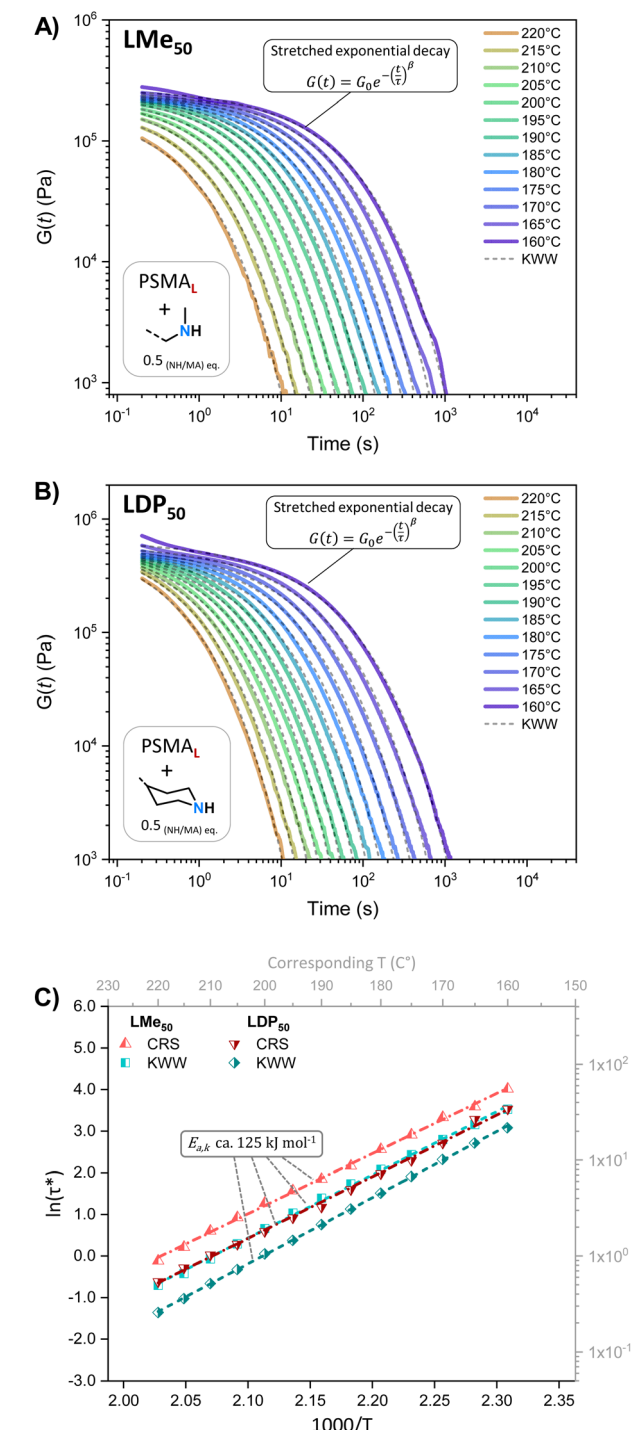


Fig. 4 Stress relaxation results of unentangled networks (A) **LMe<sub>50</sub>** and (B) **LDP<sub>50</sub>**, with their KWW stretched decays fits (dash lines). (C) Stress relaxation Arrhenius plots of networks **LMe<sub>50</sub>** and **LDP<sub>50</sub>** extracted from CRS spectra and KWW fittings.



observable difference was the higher initial  $G(t)$  values of **LDP**<sub>50</sub> compared to **LMe**<sub>50</sub> (Fig. 4A and B), mirroring its  $G'$  behavior in SAOS experiments. Their relaxation curves could then be successfully fitted to Kohlrausch–Williams–Watts ( $K_{WW}$ ) stretched exponential decays (see eqn (3)) with  $\beta$  factors

comprised between 0.4 and 0.6 (Table S5†), revealing mono-modal relaxation profiles of moderate dispersity with remarkably fast relaxation times ( $\tau_{KWW}$ ) beyond 180 °C, *i.e.*, below 10 s (see Fig. 4C or Table S6†).

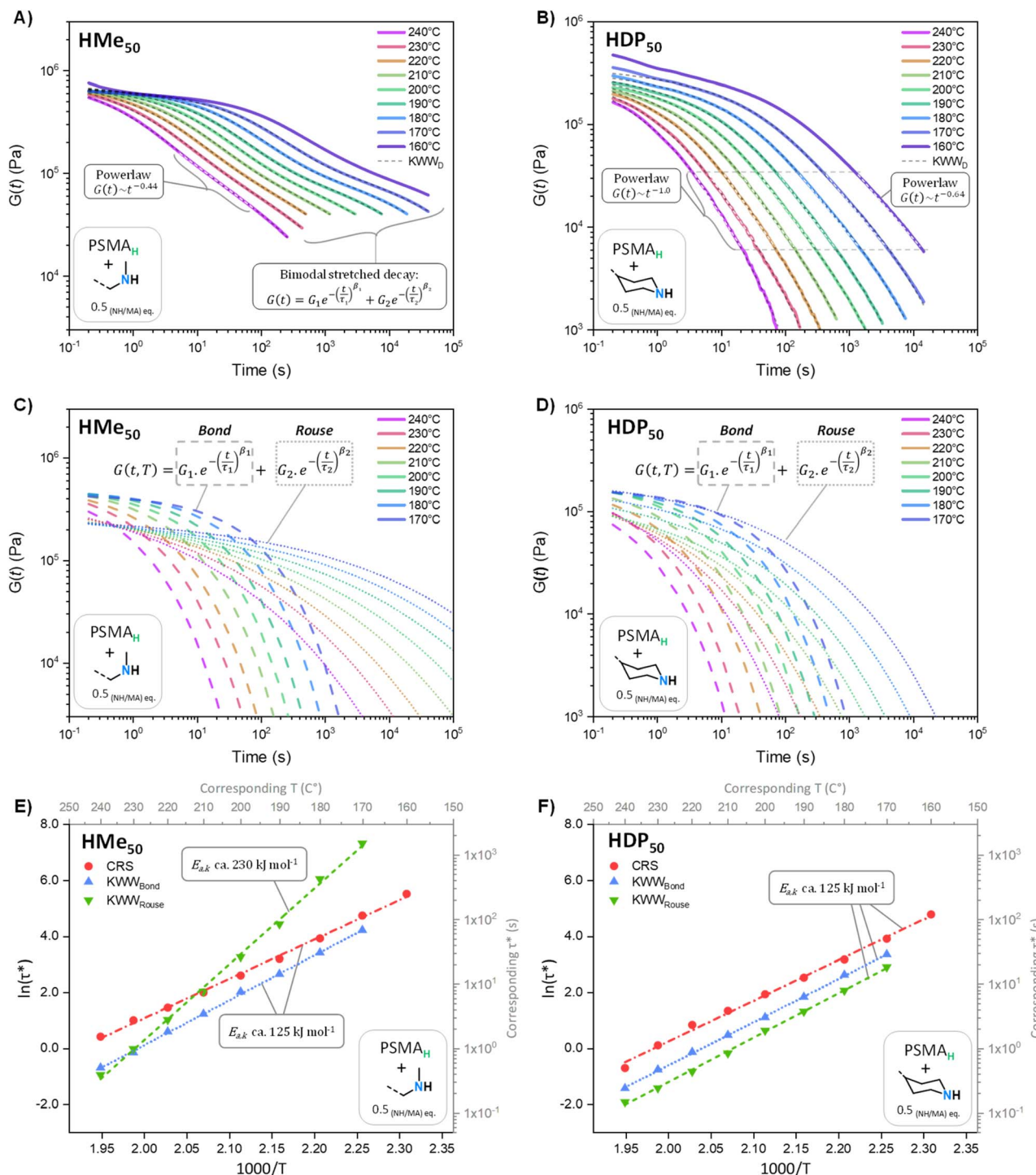


Fig. 5 (A) Stress relaxation results of network **HMe**<sub>50</sub> with representation of the Rouse power-law and its two-element KWWD ( $KWW_D$ ) decay fits (dash lines). (B) Stress relaxation results of network **HDP**<sub>50</sub> with indication of the Rouse power-law decays. (C and D) Isolated KWWD components of networks **HMe**<sub>50</sub> and **HDP**<sub>50</sub>, associated with bond dissociation-driven ( $G_1$ ,  $\tau_1$ , and  $\beta_1$ ) and Rouse-driven ( $G_2$ ,  $\tau_2$ , and  $\beta_2$ ) relaxations. (E and F) Stress relaxation Arrhenius plots ranging from 240 °C to 160 °C extracted from CRS (red circles) and the two-component KWWD fittings (separated into  $KWW_{\text{Rouse}}$  as green inverted triangles and  $KWW_{\text{bond}}$  as blue triangles) of  $\text{PSMA}_H$ -derived networks (E) **HMe**<sub>50</sub> and (F) **HDP**<sub>50</sub>.



$$G(t, T) = G_0 e^{-\left(\frac{t}{\tau_{\text{KWW}}}\right)^\beta} \quad (3)$$

$$\tau(T) = A e^{\left(\frac{E_{a,k}}{RT}\right)} \quad (4)$$

The results obtained suggest homogeneous network structures, where the dynamic bond exchange processes dominate and the influence of entanglements or supramolecular interactions is minimal. Moreover, the relaxation time distributions  $H(\lambda)$  extracted from the continuous relaxation spectra (CRS)<sup>16,55–57</sup> of the L-Series, obtained using the PyRespect software developed by Shanbhag,<sup>58</sup> also revealed monomodal relaxation time distributions without intense slow relaxation modes (Fig. S11†), corroborating the KWW analyses and yielding similar relaxation times ( $\tau$ ) and activation energies ( $E_{a,k}$ , see eqn (4), ca. 125 kJ mol<sup>−1</sup> see Fig. 4C, S12 or Table S6†).

Conversely, the relaxation profiles of the entangled H-Series PS-MMAs (Fig. 5A, B and S13†) deviated from the narrow monomodal behavior observed in the L-Series. Entangled CANs are known to develop slow relaxation modes that intensify at lower temperatures,<sup>16</sup> transitioning from monomodal relaxations towards ‘discrete Rouse’<sup>29,59</sup> multi-regime profiles governed by sticky reptation and Rouse mechanisms as follows: (R-I) initial sticky reptation and Rouse dynamics at lower temperatures that showcase the transition from the glassy state to the rubbery state following power-law decays, (R-II) a rubbery plateau modulus, (R-III) a second power-law decay associated with sticky Rouse and reptation mechanisms, and (R-IV) a terminal mono-exponential decay relaxation.

However, clear differences emerge at a glance when comparing the obtained relaxation curves of **HMe<sub>50</sub>** and **HDP<sub>50</sub>** (see Fig. 5A and B). Despite the fact that both were formulated following the same 0.5 equivalents of amine groups per anhydride crosslinkers (Table 1), **HMe<sub>50</sub>** (Fig. 5A) was only found close to exhibiting a defined power-law decay with ‘ $G(t) \sim t^{-0.44}$ ’ at 240 °C, provided that its relaxation curves seem to transition to bimodal exponential decays at decreasing temperatures. This suggests the presence of a second main relaxation mode that is significantly influenced by temperature.

In contrast, the curves of **HDP<sub>50</sub>** (Fig. 5B) mainly transition across the aforementioned ‘discrete-Rouse’ regimes R-II to R-IV, where the R-III with power-law decays is between  $G_{240^\circ\text{C}}(t)$  and

$t^{-1.0}$  and  $G(t) \sim t^{-0.68}$ . Here, it should be noted that the theoretical ‘ $G(t) = t^{-0.5}$ ’ slope was ascribed to highly entangled associative models where the influence of net-crosslinking density losses is neglected.<sup>37,38,60</sup>

Interestingly, reducing the MeHDA crosslinker content ratio [NH]/[MA] from 0.5 to 0.1 in network **HMe<sub>10</sub>** (Fig. S13C†) led to a material exhibiting the same ‘discrete-Rouse’ relaxation profile including the power law decays displayed by its DPP-derived homologue **HDP<sub>10</sub>** (Fig. S13D†) and by the more densely crosslinked **HDP<sub>50</sub>** (Fig. 5B). Thus, in line with the observations made in SAOS experiments, the structure and concentration of the secondary amine crosslinker are confirmed to influence the stress relaxation and viscoelastic profiles of PS-MMAs, which are further addressed in the present section. Still, even though the CRS analyses of both **HDP<sub>50</sub>** and **HMe<sub>50</sub>** (Fig. 5B, D and S1†) revealed similar relaxation times and activation energies ( $E_{a,k,\text{CRS}} = 117 \text{ kJ mol}^{-1}$ , Table 3), the  $H(\lambda)$  function of **HMe<sub>50</sub>** exhibited broader relaxation time distributions and incomplete relaxation at extended times, implying the existence of a slower relaxation mechanism. This bimodal behavior is still consistent with the sticky Rouse and reptation models,<sup>36–38</sup> where chain diffusion or reptation events constrained by supramolecular interactions such as hydrogen bonding or polar interactions can dominate relaxation dynamics at longer times.<sup>27,59</sup> In view of those results, the whole H-Series was fitted to a two-element KWW (KWW<sub>D</sub>) decay as follows (eqn (5)):

$$G(t, T) = G_1 e^{-\left(\frac{t}{\tau_1}\right)^{\beta_1}} + G_2 e^{-\left(\frac{t}{\tau_2}\right)^{\beta_2}} \quad (5)$$

Surprisingly, the  $\beta_1$  values, found for the faster flowing components of the entire H-Series, were between 0.4 and 0.6 (Table S7†), matching the ranges of the single  $\beta$  found in the monomodal relaxation of the L-Series. In contrast, the value for the second and slower component yielded  $\beta_2$  ranges between 0.2 and 0.3 (Table S8†), which revealed a complex relaxation landscape composed of an exceptionally disperse population of relaxation events. These results indicate that both the apparent bimodal curves of **HMe<sub>50</sub>** and ‘discrete-Rouse’ curves of **HMe<sub>10</sub>**, **HDP<sub>10</sub>** and **HDP<sub>50</sub>** can be rationalized as a result of the overlapping of two main disperse relaxation modes (Fig. 5C, D and S14†). The presence of two main relaxation modes has been reported in materials with various exchange reaction

Table 3 Rheological properties of H-Series PS-MMA networks obtained via stress relaxation measurements

Material	$\tau_{220^\circ\text{C}}^a$ (s)			$\tau_{180^\circ\text{C}}^a$ (s)			$E_{a,k}^b$ (kJ mol <sup>−1</sup> )		
	CRS	Bond	Rouse	CRS	Bond	Rouse	CRS	Bond	Rouse
<b>HMe<sub>10</sub></b>	6	3	2	66	42	24	$117 \pm 1.8$	$126 \pm 1.2$	$129 \pm 1.4$
<b>HMe<sub>50</sub></b>	4	2	1	51	30	425	$117 \pm 2.1$	$133 \pm 2.6$	$229 \pm 5.5$
<b>HDP<sub>10</sub></b>	2	1	0.4	33	12	7	$119 \pm 3.3$	$130 \pm 0.8$	$135 \pm 2.3$
<b>HDP<sub>50</sub></b>	2	1	0.4	24	14	8	$121 \pm 2.9$	$130 \pm 1.7$	$132 \pm 1.8$

<sup>a</sup> Relaxation times  $\tau$  at 220 or 180 °C obtained from CRS  $H(\lambda)$  maxima and both bond-driven and Rouse-driven KWW<sub>D</sub> components, where  $\tau_{\text{bond}} = \tau_1$  and  $\tau_{\text{Rouse}} = \tau_2$ . <sup>b</sup> Kinetic activation energy ( $E_{a,k}$ , see equation eqn (4), of the stress relaxation of the network calculated from the CRS  $H(\lambda)$  maxima and both bond-driven and Rouse-driven KWW<sub>D</sub> components.



mechanisms,<sup>61</sup> coexistence of different dynamic chemistries,<sup>62,63</sup> or a defined population of catalyzed dynamic cross-links.<sup>10,64</sup> In our case, no other plausible reaction mechanism could be confirmed *via* DFT calculations. Even though activation energies in the range of those of the slow mode found in **HMe<sub>50</sub>** (*ca.* 230 kJ mol<sup>-1</sup>, Fig. 5E) have been reported,<sup>39,65,66</sup> such elevated value could also indicate that an additional physical phenomenon is contributing to the flow rate gains at increasing temperatures.

These findings strengthen the hypothesis of a coexistence of both a distribution of faster relaxations that are predominantly driven by fast bond dissociations ( $\tau_{\text{bond}} = \tau_1$ ) and a second array of relaxation events governed by the Rouse time of reptating entangled chain strands ( $\tau_{\text{Rouse}} = \tau_2$ )<sup>28,29</sup> defining the timescale for terminal relaxation in these systems ( $\tau_{\text{TR}}$ ).<sup>67</sup>

At the same time, such chain Rouse times can see themselves strengthened by accumulative supramolecular interactions that act as a further layer of intrinsic reptation stickers.<sup>26,68,69</sup> Considering that the frictional drag coefficient, associated with the stickers acting over an entangled chain segment undergoing reptation, is proportional to  $\tau_{\text{Rouse}}$ ,<sup>29</sup> efficient supramolecular interactions involving amides, carboxylic acids, dissociated amines, or anhydrides are likely to significantly impair these slow relaxation modes (Fig. 6A).<sup>59</sup>

We then hypothesized that, in a situation where entangled chain segment motions would be significantly restrained by intense reptation phenomena (*e.g.*, in **HMe<sub>50</sub>**), the evolution of  $\tau_{\text{Rouse}}$  would become substantially more pronounced than that of  $\tau_{\text{bond}}$ , or in other words:  $E_{\text{a},\text{k},\text{Rouse}} \gg E_{\text{a},\text{k},\text{bond}}$ . Consequently, as temperature decreases, sticky reptation constrained relaxation events would intensify at a much faster rate than bond dissociation-driven relaxations, leading to bimodal relaxation profiles where sticky Rouse relaxation regimes ultimately decouple from faster bond exchange-driven relaxation events free of reptation restrictions. This situation would explain why

**HMe<sub>50</sub>**, as the only densely crosslinked entangled network derived from the less-hindered amines within the MeHDA crosslinker (Fig. 6B), resulted in stronger supramolecular reptation constraints than its bulkier DPP-derived counterpart (**HDP<sub>50</sub>**). Such structure–property relationship not only accounts for the formulation dependence of **HMe<sub>50</sub>**'s bimodal stress relaxation profile (Fig. 5A) but also elucidates the reason behind the observed higher and invariable  $G'_p$  values, as the network elasticity was being reinforced by stronger supramolecular interactions. Therefore, as indicated in Table 3 and Fig. 5E and F, the previously discussed KWW<sub>D</sub> analysis essentially captured discrete  $\tau$  and  $E_{\text{a},\text{k}}$  of either a dominant 'bond' dissociation or 'sticky Rouse' reptation restrained flow components. In fact, despite the differences observed on the  $\tau_{\text{bond}}$  values across the entire **H**-Series, all  $E_{\text{a},\text{k},\text{bond}}$  values were found to be between 117 and 133 kJ mol<sup>-1</sup>. Likewise, the  $E_{\text{a},\text{k},\text{Rouse}}$  extracted from the three 'discrete-Rouse' materials (*i.e.*, **HDP<sub>50</sub>**, **HDP<sub>10</sub>** and **HMe<sub>10</sub>**, Fig. 5B, C, D and S13†) is in close proximity to the  $E_{\text{a},\text{k},\text{KWW}}$ ,  $E_{\text{a},\text{k},\text{bond}}$  and  $E_{\text{a},\text{k},\text{CRS}}$  of the **L**-Series PS-MMAs (Tables 3 and S6†).

These observations indicate that the power-law regime (found in **HMe<sub>10</sub>**, **HDP<sub>10</sub>** and **HDP<sub>50</sub>**) seems to root in strong synergies shared between the  $E_{\text{a},\text{k}}$  of bond and reptation driven mechanisms. Consequently, the system's main relaxation mechanism follows a smooth transition from bond- to reptation-driven over a given time window. In contrast, **HMe<sub>50</sub>** showed a significant mismatch between its bond and Rouse  $E_{\text{a},\text{k}}$  (Table 3), and therefore its relaxation curves adopted two-element bimodal profiles instead of power-law decays following  $G(t) \sim t^{0.5}$ .

In order to confirm the non-covalent or kinetic nature of these observations, benzoic acid (BzOH), *p*-toluenesulfonic acid (pTSOH), zinc acetate (ZnAc<sub>2</sub>) or 7-methyl-1,5,7-triazabicyclo(4.4.0)dec-5-ene (MeTBD) were introduced in the formulation of four different **HMe<sub>50</sub>** samples (Table S3 and

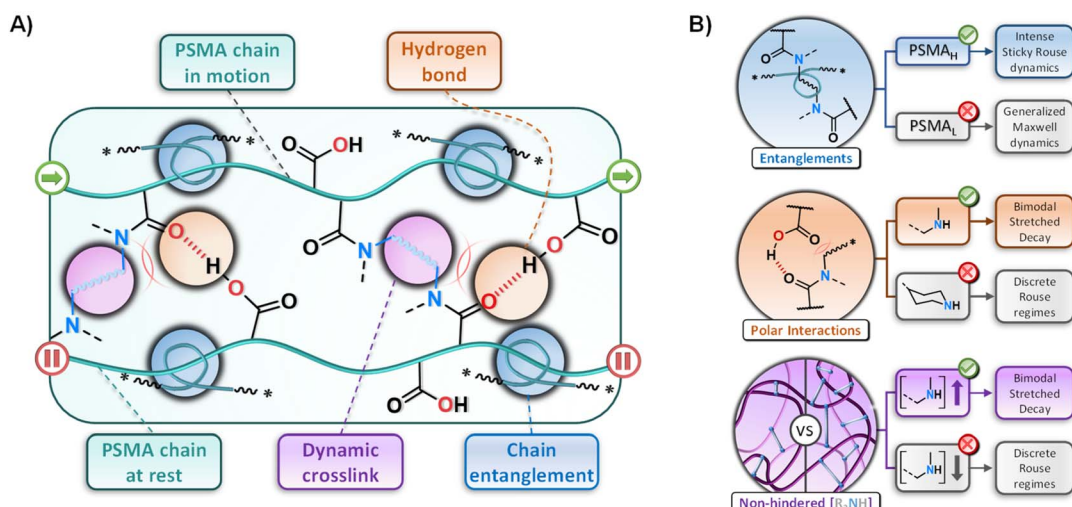


Fig. 6 A) Schematic representation depicting the main covalent and supramolecular interactions leading to high reptation drag coefficients on the sticky reptation of chain segments. (B) Chemical and physical interactions across PSMA-chain segments in PS-MMAs, revealing the composition requirements for a PS-MMA to develop a discrete bimodal stress relaxation profile and separate from 'discrete Rouse' modes. From top to bottom: entanglements, non-hindered supramolecular interactions and non-hindered amine derived crosslink density.



Scheme S3†) jointly to the **PSMA<sub>H</sub>** beads, matching 0.25 equivalents of acid/base per amine group to be used in the formulation. These polar molecules, collectively referred to as 'external reptation stickers', were chosen to evaluate their impact on both bond and Rouse relaxation components of **HMe<sub>50</sub>** when doped with mild or strong Brønsted acids (BzOH and pTSOH, respectively), Lewis acids (ZnAc<sub>2</sub>) or non-nucleophilic organic bases (MeTBD)

These polar compounds, when dispersed in the PS-MMA matrix, are expected to physically interact with polar moieties,<sup>70,71</sup> such as the carboxylic acids, amides or amines within the doped **HMe<sub>50</sub>** samples, establishing or stimulating strong polar or ionic interactions. If our initial hypothesis were to be correct, these additional external stickers should only further impair sticky reptation and Rouse mechanisms, leading only to marginal effects on bond-controlled relaxation kinetics. Once the  $T_g$ ,  $T_{d2\%}$  and gel contents of the doped **HMe<sub>50</sub>** networks were measured to ensure they shared comparable basic thermal and structural properties to those of neat **HMe<sub>50</sub>** (Tables S4†), their SAOS and stress relaxation behavior were analyzed, following the same methodologies used for the H-Series PS-MMA (Fig. S8, S17–S20 and Tables S10–S13†).

As expected, the analysis of stress relaxation experiments on those doped **HMe<sub>50</sub>** samples (Fig. S17–S20†) showed that Brønsted/Lewis acid (*i.e.*, BzOH, pTSOH, or ZnAc<sub>2</sub>) species

significantly increased the reptation relaxation times without major effects on their activation energies (Fig. 7A and Table S13†). In contrast and as predicted, the bond-driven and CRS-fitted  $\tau$  and  $E_{a,k}$  values were not severely affected (Fig. 7B, S20 and Table S13†), with the exception of the ionic ZnAc<sub>2</sub>, which seemed to have a mild negative effect on the monoamide dissociation equilibrium. The only minor reduction on  $\tau_{\text{Rouse}}$  values was observed in the PS-MMA doped with basic stickers (*i.e.*, MeTBD), where the base is expected to interfere with polar interactions between carboxylic acids and amides in their vicinity.

Interestingly, a strong base like MeTBD did not significantly alter any thermodynamic or kinetic parameters, suggesting that PS-MMA do not follow base-catalyzed mechanisms.<sup>42</sup> Additionally, extrinsic acidic stickers consistently decreased the networks' overall crosslink densities, as evidenced by reduced  $G'$  and  $G_0$  values (Fig. S8, S17 and Table S10†), as they interfered with the amine crosslinkers during the curing of the PS-MMA. In fact, the strength of Brønsted acids seemed to greatly influence both their modulus losses and the extent of their effect on network relaxations. Thus, consider that the  $pK_a$  value of aprotic solvents, such as acetonitrile, and of acyclic aliphatic ammonium salts of secondary amines is 19.<sup>50,72</sup> Then, the  $pK_a$  values of BzOH and pTSOH (*i.e.*, 22 and 8, respectively)<sup>50</sup> point to more numerous and stronger ionic acid–amine interactions that

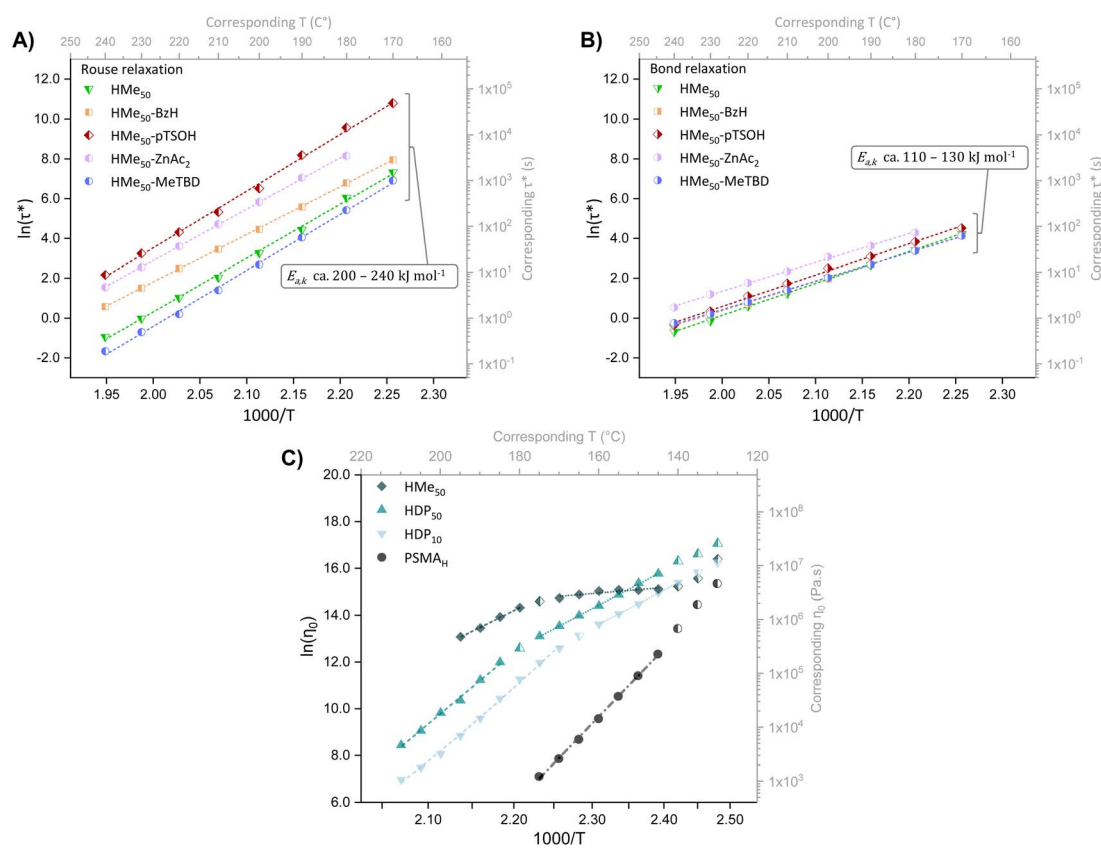


**Fig. 7** (A) Stress relaxation Arrhenius plots of **HMe<sub>50</sub>** samples doped with external reptation stickers depicting Rouse-driven relaxations extracted from KWW<sub>D</sub> decay fittings and (B) bond-driven relaxations extracted from KWW<sub>D</sub> fittings (see Fig. S20† for individual plots). (C) Arrhenius plot of the zero-shear viscosity evolution calculated from creep experiments of the H-Series monoamide PS-MMA networks: **HMe<sub>50</sub>** (diamonds), **HDP<sub>10</sub>** (upright triangles) and **HDP<sub>50</sub>** (inverted triangles) with their **PSMA<sub>H</sub>** as reference (circles).



occur only in the pTSOH-doped **HMe<sub>50</sub>**. Then, pTSOH would lead to notably higher drops in moduli and  $\tau_{\text{Rouse}}$  when compared to BzOH-doped **HMe<sub>50</sub>** or neat **HMe<sub>50</sub>** PS-MMAs.

**Macroscopic flow assessment via creep analysis.** In order to analyze the impact of both standard ‘discrete-Rouse’ and bimodal-Rouse regimes, the terminal flow behavior of PS-MMAs was monitored by following the creep compliance under constant shear stress ( $J(t) = \gamma(T, t)/\sigma$ ) in the linear regime (Fig. S21†). It is reasonable to think that the slow reptation restrained relaxations observed in **HMe<sub>50</sub>** would greatly affect the evolution of its zero shear viscosity ( $\eta_0$ ) with temperature (see eqn (6)).

$$\eta_0(T) = \left( \frac{dJ(T, t)}{dt} \right)^{-1} = A_\eta e^{\frac{E_{a,v}}{RT}} \quad (6)$$

As expected, discrete-Rouse materials such as **HDP<sub>10</sub>** or **HDP<sub>50</sub>** revealed two discrete steady flow regimes ascribed by reptation constrained and reptation-free flow states (Fig. 7C).<sup>16</sup> Both of them are evidenced by their two distinct viscous flow activation energies ( $E_{a,v}$ ) in the range of 140 kJ mol<sup>-1</sup> for creep **Regime I**, when affected by Rouse dynamics, and 260 kJ mol<sup>-1</sup> for creep **Regime II** as they enter truly terminal viscous flow. In that terminal regime, PS-MMAs reached  $E_{a,v}$  values closer to that of non-crosslinked **PSMA<sub>H</sub>** on its terminal flow state (Table S14†). **HMe<sub>50</sub>**, instead, showed an initial  $\eta_0$  plateau heavily constrained by reptation mechanisms that lead to an extremely low  $E_{a,v}$  of 22 kJ mol<sup>-1</sup>, which progressively increased to 155 kJ mol<sup>-1</sup> beyond 160 °C. This feature, observed on highly crosslinked and entangled MeHDA-derived PS-MMAs, points towards an exploitable strategy to develop tailorabile creep resistant monoamide-CANs.

### (Re)processing of PS-MMAs via injection molding

All experiments in the previous section showed that the terminal flow rates and relaxation speeds of the ‘discrete-Rouse’ PS-MMAs greatly exceed those of previously reported **PSMA**-derived monoester CANs and seemed to be less dependent on

crosslink densities. However, if the material processing method were to involve a fast cooling step, the crosslinking density and cooling temperatures were expected to become relevant factors that are necessary to be considered. As seen in the DFT calculations performed (*vide supra*) and the fast gelation times observed during the synthesis of PS-MMAs, high crosslinking degrees translate into a dense population of amines at stake and excessively fast crosslinking density regeneration upon cooling.

A processing technique where this effect can be easily observed is injection molding, where the heated material is forced to flow inside a cooled mold. Therefore, to gain insight into the influence of the crosslink density on these processes, injection molding experiments were performed using a lab-scale injection molding machine operating at an injection pressure of 8 bar with a rectangular mold (63.5 mm × 12.5 mm × 3.15 mm), using the faster flowing ‘discrete-Rouse’ materials **HDP<sub>50</sub>** and **HDP<sub>10</sub>** for this purpose. To ensure that the **H**-Series PS-MMAs could withstand short-term exposure to air at elevated temperatures (e.g.,  $T = 280$  °C;  $t \leq 10$  min), TGA experiments were performed (Fig. S4D and S5C†). Once the materials’ integrity during the processing time was indeed guaranteed, an initial injection experiment was performed using a finely ground **HDP<sub>50</sub>** sample ( $\Phi < 1$  mm), preheated at 280 °C for 2 minutes and subsequently injected into a rectangular-bar mold (63.5 mm × 12.5 mm × 3.15 mm) set at 80 °C (Fig. 8A).

As can be observed in Fig. 8A, the injected material experienced severe extrudate melt fracture and incomplete mold filling. Further decreasing the crosslinking density by selecting **HDP<sub>10</sub>** afforded more intense viscosity drops, adequate for the material to at least flow inside the mold before it vitrifies and creates a kind of adhered-particle agglomerate<sup>73</sup> (Fig. 8B). Mold temperatures that are much higher than the network’s  $T_g$  (i.e., mold set at 180 vs. 127 °C for the  $T_g$ ) created surface distortions due to the thermal history of the material (Fig. 8C).

Finally, decreasing the mold temperature to 140 °C yielded a homogeneous specimen with a uniform surface. However, as can be observed in Fig. 8D, the injection pressure limit, set by

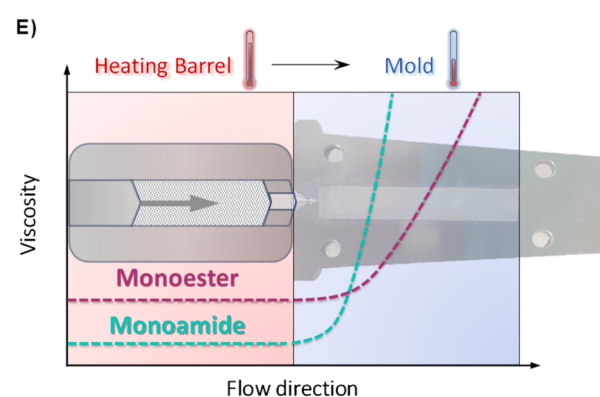
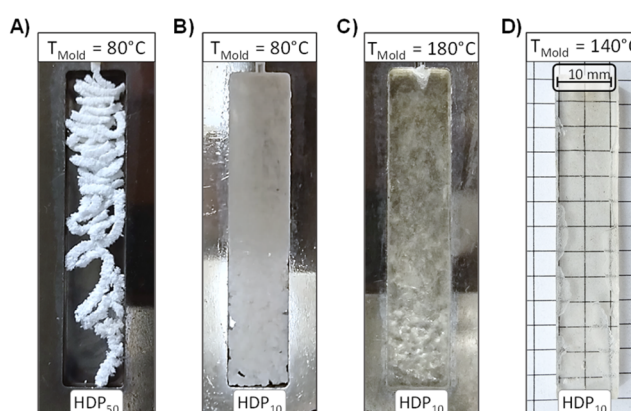


Fig. 8 Pictures of injection molding experiments (63.5 mm × 12.5 mm × 3.15 mm) performed on samples pre-heated at 280 °C. (A) **HDP<sub>50</sub>** injected into the mold set at 80 °C, (B) **HDP<sub>10</sub>** injected into the mold set at 80 °C, (C) **HDP<sub>10</sub>** injected into the mold set at 180 °C and (D) **HDP<sub>10</sub>** injected into the mold set at 140 °C. (E) Diagram of the viscosity evolution in the injection flow direction during the injection of monoester and monoamide samples.



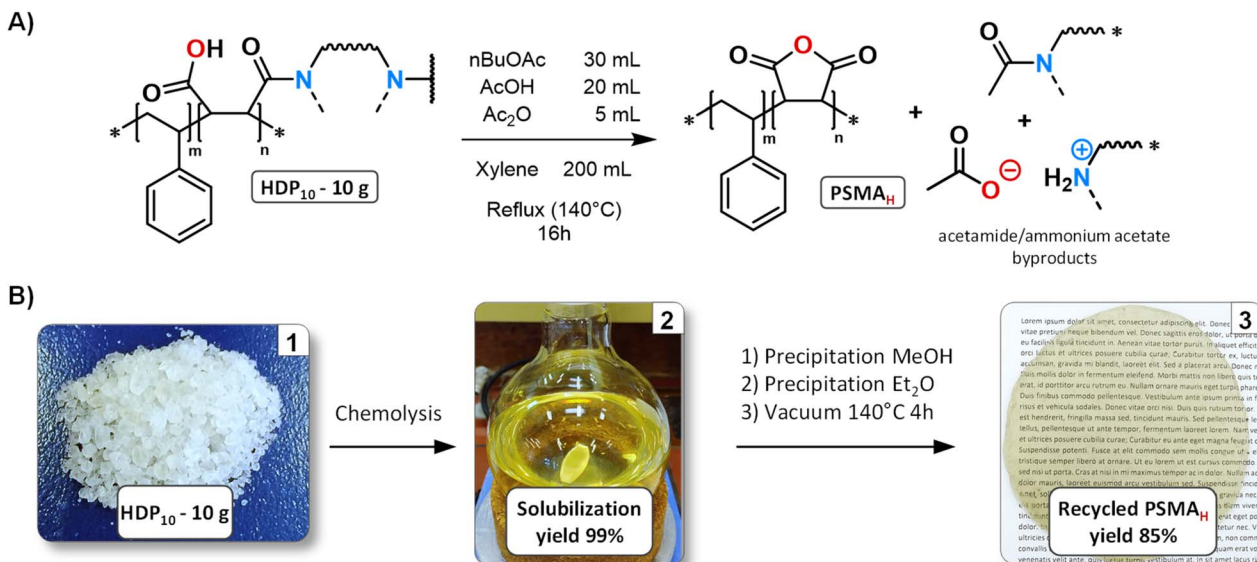


Fig. 9 (A) Schematic representation of the chemical recycling *via* chemolysis performed on 10 g of HDP<sub>10</sub>. (B1) Shredded HDP<sub>10</sub> sample used in the study. (B2) Recycled PSMA<sub>H</sub> and DPP-amide/DPP-salt byproduct solution in xylene after its chemolysis. (B3) Chemically recycled PSMA<sub>H</sub> sample.

the maximum operating pressure of the benchtop setup (8 bar, Fig. S22†), was insufficient to completely evacuate the air originally trapped within the mold before the material's vitrification, leading to small surface deformations near the edges of the sample. Nevertheless, the injected sample's unchanged  $T_g$  (Fig. S23A†) and the slow decay of  $G'$  beyond this temperature, as observed *via* shear DMA analysis (Fig. S23B†), demonstrated the integrity of the PS-MMA CAN and its suitability for high-temperature processing.

### Chemical recycling of PS-MMAs

As the last part of this study, we targeted a chemical recycling process with the aim to recovering the PSMA<sub>H</sub> used in the synthesis of HDP<sub>10</sub> (Fig. 9A). After isolation and purification, the recuperated PSMA copolymer could then be potentially repurposed or used again in the synthesis of new PS-MMAs, extending the lifetime of its components beyond that achievable by only physically reprocessing it.

With this target in mind, 10 g of ground HDP<sub>10</sub> (Fig. 9B1) from pressed plates (190 °C for 10 min and 7 MPa) was dissolved in a mixture of 200 mL of xylene, 30 mL of butyl acetate (nBuOAc), 20 mL of acetic acid 98% (AcOH) and 5 mL of acetic anhydride (Ac<sub>2</sub>O) set under reflux in a Soxhlet extraction setup at 140 °C (Fig. 9A). During this step, butyl acetate and acetic anhydride were added to trap and separate the dissociated amines by forming tertiary acetamides or ammonium salts that would not regenerate the lost monoamides. After 16 h at reflux, the recycled PSMA<sub>H</sub> (PSMA<sub>H-Rec</sub>) was then separated from the obtained solution in xylene (39.2 mg mL<sup>-1</sup>, Fig. 9B2) by precipitating it using 200 mL of cold methanol.

The obtained yellow polymer was dried at 80 °C for 1 h and at 140 °C for 4 h under vacuum. Lastly, the dry sample was then dissolved again in 100 mL of THF, filtered by gravity,

precipitated again using 300 mL of cold diethyl ether and dried using the same conditions as used during the previous step. The precursor PSMA copolymer could be recovered with a 85% yield as an off-yellow transparent amorphous soluble polymer (Fig. 9B3). The recovered PSMA<sub>H-Rec</sub> displayed comparable structural aspects as assessed by FTIR and <sup>1</sup>H-NMR (see Fig. S24 and S25†) when compared to the virgin PSMA<sub>H</sub> with the exception of the yellow coloration and an increase in the  $M_w$  from 183 to 345 kg mol<sup>-1</sup>, as measured by size exclusion chromatography (Fig. S1†). Such molar mass increase has been attributed to PSMA chain couplings triggered by residual diamines that remained within the PSMA<sub>H-Rec</sub> polymer.

### Conclusions

This study successfully explored the design, synthesis, and characterization of poly(styrene-*co*-maleamic acid) (PS-MMA) covalent adaptable networks (CANs) as a novel class of thermally reprocessable materials based on monoamide dynamic chemistry. By utilizing the reactivity of secondary diamines with PSMA copolymers and controlling the amine-to-anhydride ratio, we developed tunable network architectures that enable fine adjustment of crosslink density, reprocessability, and mechanical properties. The introduction of tertiary amides provided a robust framework for creating CANs with enhanced thermal stability and dynamic behavior.

DFT calculations revealed the enthalpically favored reassociation of monoamide bonds, aligning with the dissociation behavior observed in High-Temperature FTIR analyses.

The reported findings confirm the unique dissociative exchange chemistry of PS-MMAs. Rheological assessments further demonstrated structure-dependent profiles driven by the interplay of crosslink density, chain entanglements, and amine crosslinker architecture. These networks exhibited



a combination of fast dissociation-driven relaxation and slower reparation-driven dynamics, allowing tailored flow and stress relaxation behavior suitable for diverse processing conditions. Thermal analyses confirmed the remarkable resilience of PS-MMAs, maintaining dynamic properties and structural integrity at temperatures up to 280 °C, outperforming conventional CAN systems. Furthermore, chemical recycling experiments showcased the sustainability of PS-MMAs, enabling efficient recovery of their PSMA precursor copolymer while preserving their functionality, underscoring the potential for these networks to integrate into a circular polymer economy and extend the material lifecycle.

In summary, PS-MMAs represent a significant advancement in dynamic covalent polymer networks, combining high-performance mechanical and thermal properties with reprocessability and recyclability. These findings highlight their potential for demanding industrial applications where thermal stability, reprocessability, and sustainability are critical, providing a pathway for environmentally conscious material innovation.

## Data availability

The data supporting this article have been included as part of the ESI.† The raw and processed data required to reproduce these findings are available upon request to the corresponding author.

## Conflicts of interest

The authors have no conflict of interest to declare.

## Acknowledgements

This project received funding from the European Union's Horizon 2020 research and innovation program under the Marie Skłodowska-Curie Grant agreement No. 860911 (VITRIMAT). The NMR expertise center (Ghent University) is also acknowledged for providing support and access to NMR infrastructure funded by the Research Foundation - Flanders (I006920N) and the Bijzonder Onderzoeksfonds (BOF.BAS. 2022.0023.01). The authors thank Bernhard De Meyer for providing technical support, Croda and Aurorium (formerly Polyscope) for kindly providing samples that were used in this project. Likewise, the authors express their gratitude to Dr Jérémie Odent and Prof. Dr Jean-Marie Raquez for their assistance during the injection molding tests. Lastly, we acknowledge Loc Tan Nguyen and Dr Adrià Roig for the fruitful discussions held during the duration of this study.

## References

- 1 C. J. Kloxin, T. F. Scott, B. J. Adzima and C. N. Bowman, *Macromolecules*, 2010, **43**, 2643–2653.
- 2 D. Montarnal, M. Capelot, F. Tournilhac and L. Leibler, *Science*, 2011, **334**, 965–968.
- 3 M. Podgórski, B. D. Fairbanks, B. E. Kirkpatrick, M. McBride, A. Martinez, A. Dobson, N. J. Bongiardina and C. N. Bowman, *Adv. Mater.*, 2020, **32**, 1906876.
- 4 J. M. Winne, L. Leibler and F. E. Du Prez, *Polym. Chem.*, 2019, **10**, 6091–6108.
- 5 V. Zhang, B. Kang, J. V. Accardo and J. A. Kalow, *J. Am. Chem. Soc.*, 2022, **144**, 22358–22377.
- 6 A. V. Karatrantos, O. Couture, C. Hesse and D. F. Schmidt, *Polymers*, 2024, **16**, 1373.
- 7 F. Van Lijsebetten, J. O. Holloway, J. M. Winne and F. E. Du Prez, *Chem. Soc. Rev.*, 2020, **49**, 8425–8438.
- 8 O. R. Cromwell, J. Chung and Z. Guan, *J. Am. Chem. Soc.*, 2015, **137**, 6492–6495.
- 9 M. Delahaye, J. M. Winne and F. E. Du Prez, *J. Am. Chem. Soc.*, 2019, **141**, 15277–15287.
- 10 M. Delahaye, F. Tanini, J. O. Holloway, J. M. Winne and F. E. Du Prez, *Polym. Chem.*, 2020, **11**, 5207–5215.
- 11 H. Zhang, S. Majumdar, R. A. T. M. van Benthem, R. P. Sijbesma and J. P. A. Heuts, *ACS Macro Lett.*, 2020, **9**, 272–277.
- 12 M. Podgórski, S. Mavila, S. Huang, N. Spurgin, J. Sinha and C. N. Bowman, *Angew. Chem., Int. Ed.*, 2020, **59**, 9345–9349.
- 13 Y. Chen, H. Zhang, S. Majumdar, R. A. T. M. van Benthem, J. P. A. Heuts and R. P. Sijbesma, *Macromolecules*, 2021, **54**, 9703–9711.
- 14 F. Van Lijsebetten, Y. Spiesschaert, J. M. Winne and F. E. Du Prez, *J. Am. Chem. Soc.*, 2021, **143**, 15834–15844.
- 15 R. Wink, S. Majumdar, R. A. T. M. van Benthem, J. P. A. Heuts and R. P. Sijbesma, *Polym. Chem.*, 2023, **14**, 4294–4302.
- 16 A. Hernández, T. Maiheu, E. Drockenmuller, D. Montarnal, J. M. Winne and F. E. Du Prez, *Chem. Mater.*, 2024, **36**, 7487–7503.
- 17 W. Denissen, M. Droebeke, R. Nicolaï, L. Leibler, J. M. Winne and F. E. Du Prez, *Nat. Commun.*, 2017, **8**, 14857.
- 18 J. L. Self, N. D. Dolinski, M. S. Zayas, J. Read de Alaniz and C. M. Bates, *ACS Macro Lett.*, 2018, **7**, 817–821.
- 19 A. R. Padwa, Y. Sasaki, K. A. Wolske and C. W. Macosko, *J. Polym. Sci., Part A: Polym. Chem.*, 1995, **33**, 2165–2174.
- 20 B. R. Elling and W. R. Dichtel, *ACS Cent. Sci.*, 2020, **6**, 1488–1496.
- 21 A. Jourdain, R. Asbai, O. Anaya, M. M. Chehimi, E. Drockenmuller and D. Montarnal, *Macromolecules*, 2020, **53**, 1884–1900.
- 22 O. Anaya, A. Jourdain, I. Antoniuk, H. Ben Romdhane, D. Montarnal and E. Drockenmuller, *Macromolecules*, 2021, **54**, 3281–3292.
- 23 B. J. Adzima, H. A. Aguirre, C. J. Kloxin, T. F. Scott and C. N. Bowman, *Macromolecules*, 2008, **41**, 9112–9117.
- 24 J. J. Lessard, K. A. Stewart and B. S. Sumerlin, *Macromolecules*, 2022, **55**, 10052–10061.
- 25 I. Mahmad Rasid, A. Rao, N. Holten-Andersen and B. D. Olsen, *Macromolecules*, 2022, **55**, 6056–6066.
- 26 M. Ahmadi, L. G. D. Hawke, H. Goldansaz and E. van Ruymbeke, *Macromolecules*, 2015, **48**, 7300–7310.
- 27 L. M. Fenimore, M. J. Suazo and J. M. Torkelson, *Macromolecules*, 2024, **57**, 2756–2772.



28 L. Leibler, M. Rubinstein and R. H. Colby, *Macromolecules*, 1991, **24**, 4701–4707.

29 R. G. Ricarte and S. Shanbhag, *Macromolecules*, 2021, **54**, 3304–3320.

30 D. J. Plazek and V. M. O'Rourke, *J. Polym. Sci., Part A-2*, 1971, **9**, 209–243.

31 M. K. Singh, M. Hu, Y. Cang, H.-P. Hsu, H. Therien-Aubin, K. Koynov, G. Fytas, K. Landfester and K. Kremer, *Macromolecules*, 2020, **53**, 7312–7321.

32 J. Noolandi, G. Slater and G. Allegra, *Makromol. Chem., Rapid Commun.*, 2003, **8**, 51–58.

33 S. F. Edwards, H. Takano and E. M. Terentjev, *J. Chem. Phys.*, 2000, **113**, 5531–5538.

34 W. L. Vandoolaeghe and E. M. Terentjev, *J. Chem. Phys.*, 2005, **123**, 034902.

35 W. L. Vandoolaeghe and E. M. Terentjev, *J. Phys. A: Math. Theor.*, 2007, **40**, 14725–14744.

36 S. Wu and Q. Chen, *Macromolecules*, 2022, **55**, 697–714.

37 X. Cui, N. Jiang, J. Shao, H. Zhang, Y. Yang and P. Tang, *Macromolecules*, 2023, **56**, 772–784.

38 J. Xia, J. A. Kalow and M. Olvera de la Cruz, *Macromolecules*, 2023, **56**, 8080–8093.

39 L. T. Nguyen, F. Portone and F. E. Du Prez, *Polym. Chem.*, 2024, **15**, 11–16.

40 S. Su, F.-S. Du and Z.-C. Li, *Org. Biomol. Chem.*, 2017, **15**, 8384–8392.

41 B. Qin, S. Liu, Z. Huang, L. Zeng, J.-F. Xu and X. Zhang, *Nat. Commun.*, 2022, **13**, 7595.

42 J. Zhang, Y. Zhou, S. Ma and F. Zhou, *Green Chem.*, 2024, **26**, 3368–3377.

43 F. Neese, *Wiley Interdiscip. Rev. Comput.*, 2012, **2**, 73–78.

44 T. Yanai, D. P. Tew and N. C. Handy, *Chem. Phys. Lett.*, 2004, **393**, 51–57.

45 A. Hellweg and D. Rappoport, *Phys. Chem. Chem. Phys.*, 2015, **17**, 1010–1017.

46 V. Barone and M. Cossi, *J. Phys. Chem. A*, 1998, **102**, 1995–2001.

47 V. Ásgeirsson, B. O. Birgisson, R. Bjornsson, U. Becker, F. Neese, C. Ripplinger and H. Jónsson, *J. Chem. Theory Comput.*, 2021, **17**, 4929–4945.

48 K. Fukui, *Acc. Chem. Res.*, 1981, **14**, 363–368.

49 F. F. Becker, C. Mukhopadhyay, L. Hackfeld, I. Banik and B. K. Banik, *Bioorg. Med. Chem.*, 2000, **8**, 2693–2699.

50 A. Kütt, S. Tshepelevitsh, J. Saame, M. Lõkov, I. Kaljurand, S. Selberg and I. Leito, *Eur. J. Org. Chem.*, 2021, **2021**, 1407–1419.

51 M. Delahaye, J. M. Winne and F. E. Du Prez, *J. Am. Chem. Soc.*, 2019, **141**, 15277–15287.

52 T. Maiheu, J. Debuyck, F. Van Lijsebetten, A. Hernández and F. E. Du Prez, *Eur. Polym. J.*, 2024, **210**, 112998.

53 L. M. Fenimore, B. Chen and J. M. Torkelson, *J. Mater. Chem. A*, 2022, **10**, 1039.

54 H. Y. Song, G. Lee, S. Ahn and K. Hyun, *Korea-Aust. Rheol. J.*, 2023, **35**, 69–79.

55 L. Porath, J. Huang, N. Ramlawi, M. Derkaloustian, R. H. Ewoldt and C. M. Evans, *Macromolecules*, 2022, **55**, 4450–4458.

56 R. G. Ricarte and S. Shanbhag, *Polym. Chem.*, 2024, **15**, 815–846.

57 L. E. Porath, N. Ramlawi, J. Huang, M. T. Hossain, M. Derkaloustian, R. H. Ewoldt and C. M. Evans, *Chem. Mater.*, 2024, **36**, 1966–1974.

58 S. Shanbhag, *Macromol. Theory Simul.*, 2019, **28**, 1900005.

59 R. G. Ricarte, S. Shanbhag, D. Ezzeddine, D. Barzycki and K. Fay, *Macromolecules*, 2023, **56**, 6806–6817.

60 J. Shao, N. Jiang, H. Zhang, Y. Yang and P. Tang, *Macromolecules*, 2022, **55**, 535–549.

61 M. Guerre, C. Taplan, R. Nicolaï, J. M. Winne and F. E. Du Prez, *J. Am. Chem. Soc.*, 2018, **140**, 13272–13284.

62 J. Zhao, Z. Zhang, C. Wang and X. Yan, *CCS Chem.*, 2023, **6**, 41–56.

63 S. Maes, F. Van Lijsebetten, J. M. Winne and F. E. Du Prez, *Macromolecules*, 2023, **56**, 1934–1944.

64 F. Van Lijsebetten, K. De Bruycker, E. Van Ruymbeke, J. M. Winne and F. E. Du Prez, *Chem. Sci.*, 2022, **13**, 12865–12875.

65 C. Taplan, M. Guerre and F. E. Du Prez, *J. Am. Chem. Soc.*, 2021, **143**, 9140–9150.

66 M. A. Bin Rusayyis, L. M. Fenimore, N. S. Purwanto and J. M. Torkelson, *Polym. Chem.*, 2023, **14**, 3519–3534.

67 S. Shanbhag and R. G. Ricarte, *Macromol. Theory Simul.*, 2023, **32**, 2300002.

68 J. Brassinne, A. Cadix, J. Wilson and E. van Ruymbeke, *J. Rheol.*, 2017, **61**, 1123–1134.

69 N. Jiang, H. Zhang, P. Tang and Y. Yang, *Macromolecules*, 2020, **53**, 3438–3451.

70 C. Schaefer, P. R. Laity, C. Holland and T. C. B. McLeish, *Macromolecules*, 2020, **53**, 2669–2676.

71 P. C. Cai, B. Su, L. Zou, M. J. Webber, S. C. Heilshorn and A. J. Spakowitz, *ACS Cent. Sci.*, 2022, **8**, 1318–1327.

72 F. V. Lijsebetten, S. Maes, J. M. Winne and F. E. D. Prez, *Chem. Sci.*, 2024, **15**, 7061–7071.

73 Z. Shen, H. Ye, Q. Wang, M. Kröger and Y. Li, *Macromolecules*, 2021, **54**, 5053–5064.

